Eur. J. Mineral.
2017, **29**, 557–570
Published online 31 May 2017

Special issue dedicated to Zdeněk Johan

Super-reduced mineral assemblages in "ophiolitic" chromitites and peridotites: the view from Mount Carmel

Qing XIONG[1], William L. GRIFFIN[1,*], Jin-Xiang HUANG[1], Sarah E.M. GAIN[1], Vered TOLEDO[2], Norman J. PEARSON[1] and Suzanne Y. O'REILLY[1]

[1] ARC Centre of Excellence for Core to Crust Fluid Systems (CCFS) and GEMOC, Department of Earth and Planetary Sciences, Macquarie University, Sydney, NSW 2109, Australia
*Corresponding author, e-mail: bill.griffin@mq.edu.au
[2] Shefa Yamim (A.T.M.) Ltd., Netanya 4210602, Israel

Abstract: Ultrahigh-pressure (*UHP*) materials (*e.g.*, diamond, high-pressure polymorph of chromite) and super-reduced (SuR) phases (*e.g.*, carbides, nitrides, silicides and native metals) have been identified in chromitites and peridotites of the Tibetan and Polar-Urals ophiolites. These unusual assemblages suggest previously unrecognized fluid- or melt-related processes in the Earth's mantle. However, the origin of the SuR phases, and in particular their relationships with the *UHP* materials in the ophiolites, are still enigmatic. Studies of a recently recognized SuR mineral system from Cretaceous volcanics on Mt Carmel, Israel, suggest an alternative genesis for the ophiolitic SuR phases. The Mt Carmel SuR mineral system (associated with Ti-rich corundum xenocrysts) appears to reflect the local interaction of mantle-derived $CH_4 \pm H_2$ fluids with basaltic magmas in the shallow lithosphere (depths of ~30–100 km). These interactions produced desilication of the magma, supersaturation in Al_2O_3 leading to rapid growth of corundum, and phase assemblages requiring local oxygen fugacity (fO_2) gradually dropping to ~11 log units below the iron–wüstite (IW) buffer. The strong similarities between this system and the SuR phases and associated Ti-rich corundum in the Tibetan and Polar-Urals ophiolites suggest that the ophiolitic SuR suite probably formed by local influx of $CH_4 \pm H_2$ fluids within previously subducted peridotites (and included chromitites) during their rapid exhumation from the deep upper mantle to lithospheric levels. In the final stages of their ascent, the recycled peridotites and chromitites were overprinted by a shallow magmatic system similar to that observed at Mt Carmel, producing most of the SuR phases and eventually preserving them within the Tibetan and Polar-Urals ophiolites.

Key-words: podiform chromitites; super-reduced phases; Tibetan ophiolites; corundum megacrysts; $CH_4 \pm H_2$ fluids; carbon cycling; mantle redox conditions.

1. Introduction

Ophiolites are fossil lithospheric fragments, which can be generated during different stages of a Wilson cycle (*e.g.*, Bodinier & Godard, 2014). Their mantle sections are composed mainly of peridotite residues after melt extraction and other ultramafic rocks (*e.g.*, dunite, chromitite) related to melt-peridotite interaction. The redox states of these lithospheric-mantle fragments range from ~1 log unit above the quartz–fayalite–magnetite (QFM) buffer to ~4 log units below QFM (*e.g.*, Stagno *et al.*, 2013). The normal oxygen fugacity (fO_2) of the lithospheric mantle, as sampled in xenoliths, decreases with depth, due to the effect of pressure (P) on Fe^{3+}–Fe^{2+} equilibria in upper-mantle minerals (*e.g.*, Frost & McCammon, 2008; Luth & Stachel, 2014). All these estimates are more oxidizing than the iron–wüstite (IW) buffer, which marks the saturation of Fe metal in the upper mantle (*e.g.*, Frost & McCammon, 2008).

However, a striking discovery during the last decades is the occurrence of natural moissanite (SiC), carbides, nitrides, silicides and native metals (Table S1, freely available online as Supplementary Material linked to this article on the GSW website of the journal, http://eurjmin.geoscienceworld.org/) in the chromitites and peridotites of ophiolites from Tibet (China) and the Polar Urals (Russia) (Fig. 1; *e.g.*, Robinson *et al.*, 2004; Dobrzhinetskaya *et al.*, 2009; Xu *et al.*, 2015; Yang *et al.*, 2015a and b; Zhang *et al.*, 2016a). The formation and stability of moissanite requires fO_2 to be at least six orders of magnitude lower than the IW buffer (*e.g.*, Ulmer *et al.*, 1998; Golubkova *et al.*, 2016). The super-reduced (SuR) conditions are thus inconsistent with the normal oxidation state of the "ophiolitic-mantle" system, which represents shallow oceanic lithosphere.

Ultrahigh-pressure (*UHP*) phases and assemblages (summarized in Table S1) also have been separated from or observed *in situ* in chromitites and peridotites from the Tibetan and Polar-Urals ophiolites, which also contain the SuR assemblages (*e.g.*, Bai *et al.*, 1993; Robinson *et al.*, 2004; Yang *et al.*, 2007, 2015a and b; Dobrzhinetskaya *et al.*, 2009, 2014; Yamamoto *et al.*, 2009; Xu *et al.*, 2013, 2015; Howell *et al.*, 2015; McGowan *et al.*, 2015; Griffin

DOI: 10.1127/ejm/2017/0029-2646
0935-1221/17/0029-2646 $ 6.30

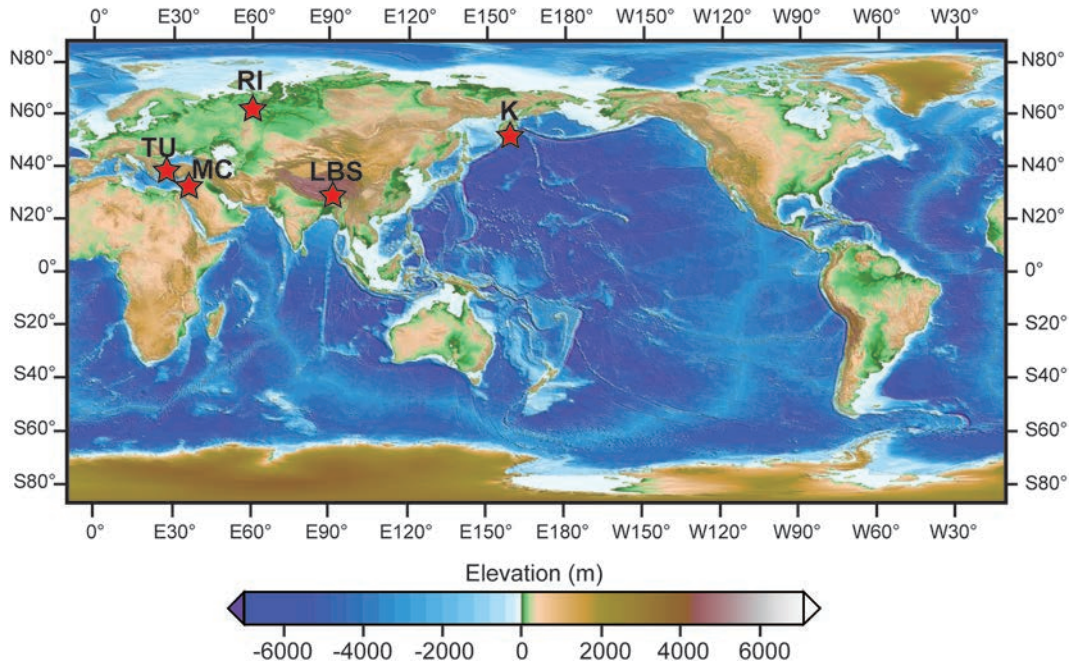

Fig. 1. Locations of reported super-reduced mineral assemblages in Luobusa (LBS, Tibet), Ray-Iz (RI, Polar Urals), Mt Carmel (MC, Israel), Kamchatka (K) and Turkey (TU). The global topography map is constructed using GMT program and elevation data from ETOPO1 Global Relief Model from National Geophysical Data Center.

et al., 2016a; Zhang *et al.*, 2016a). These *UHP* phases and textural evidence suggest derivation from depths of at least ~300 km, and probably from the Mantle Transition Zone (*e.g.*, Satsukawa *et al.*, 2015; Griffin *et al.*, 2016a; Zhang *et al.*, 2017).

Previous studies have treated the SuR phases together with the *UHP* materials, as being all derived from the very reduced Mantle Transition Zone or the deep levels of the upper mantle (Robinson *et al.*, 2004; Yang *et al.*, 2007, 2014, 2015a and b; Dobrzhinetskaya *et al.*, 2009; Zhang *et al.*, 2016a). However, there are only two unambiguous cases showing that *UHP* phases enclose SuR phases: one is the association of coesite in stishovite pseudomorphs, cubic BN, and a high-*P* polymorph of TiO_2 with αPbO_2 structure, with a SuR suite of native Fe, Ti, TiN and boron carbide (Yang *et al.*, 2007; Dobrzhinetskaya *et al.*, 2009, 2014); the other is the inclusions of Ni–Mn–Co alloys in diamond (*e.g.*, Howell *et al.*, 2015). Other SuR phases, such as moissanite, native metals, carbides, nitrides and silicides (Table S1), are found in mineral separates and have no confirmed textural connection with the *UHP* materials (*e.g.*, Robinson *et al.*, 2004; Yang *et al.*, 2014, 2015a and b; Xu *et al.*, 2015).

Recently, an assemblage of SuR phases, including the first terrestrial occurrence of tistarite (Ti_2O_3) and a suite of native metals, carbides, nitrides, silicides and amorphous carbon (Tables S1, S2), has been found in corundum xenocrysts ejected from Cretaceous volcanoes in Mount Carmel, northern Israel (Griffin *et al.*, 2016b). These SuR assemblages show clear similarities with the SuR suite from the Tibet and Polar Urals ophiolites. In this study, we use the Mt Carmel SuR assemblages to explore the genesis of the ophiolitic analogs in Tibet and the Polar Urals from a different perspective, and propose that the SuR phases in the ophiolites may not be collectively formed together with the *UHP* materials in the Mantle Transition Zone or the deep upper mantle.

2. Tibet–Polar Urals ophiolites and their *UHP*–SuR associations

2.1. Geological background

The *UHP*–SuR mineral associations have been found mainly in the chromitites and peridotites of the Luobusa ophiolite from the Yarlung Zangbo Suture Zone (south Tibet, China; *e.g.*, Yang *et al.*, 2014; Zhang *et al.*, 2016a) and the Ray-Iz ophiolite from the Ural orogenic belt (Russia; *e.g.*, Yang *et al.*, 2015a). The Luobusa ophiolite (Fig. 1) is one of many in the Yarlung Zangbo Suture Zone, which extends ~2000 km from west to east and separates Greater India from the Lhasa Block (Asia) in the north. The Yarlung Zangbo ophiolites represent "fossil" lithospheric fragments from the Neo-Tethyan oceanic lithosphere, which was mainly consumed during the India–Asia convergence in the Mesozoic/Cenozoic (*e.g.*, Hébert *et al.*, 2012). The Ray-Iz ophiolite (Fig. 1) is one of the ultramafic bodies in the early Paleozoic Uralian orogen, a ~3000 km long, N–S-trending collision belt that separates Europe from Asia (*e.g.*, Chemenda *et al.*, 1997). The Uralian ophiolites represent relict fragments of the Western Uralian oceanic lithosphere, thrust onto land during the early Paleozoic collision of the European and Asian continents (*e.g.*, Batanova *et al.*, 2011; Shmelev, 2011).

The Luobusa ophiolite (including the Luobusa, Xiangkashan and Kangjinla areas, ~70 km^2) is tectonically sandwiched between Triassic flysch sediments in the south and the Gangdese Arc batholiths or the Tertiary Luobusa conglomerate belt in the north. From north to south, it is comprised of (1) a serpentinite mélange zone with gabbroic and basaltic blocks or dykes (zircon U–Pb ages of ~130–120 Ma; Zhang *et al.*, 2016b), (2) a dunite-facies zone with mainly high-Cr# [molar $Cr^{3+}/(Cr^{3+}+Al^{3+})$] dunite and chromitite in a harzburgite framework, (3) a clinopyroxene-poor harzburgite zone with high-Cr# dunite and chromitite lenses and gabbro dykes (zircon U–Pb ages of ~160–150 Ma and ~130–120 Ma; Zhong *et al.*, 2006; Chan *et al.*, 2015; Zhang *et al.*, 2016b), and (4) a clinopyroxene-rich harzburgite or lherzolite zone with rare lenses of low-Cr# dunite and disseminated chromitite. Previous studies have proposed that the Luobusa ophiolite initially formed in a mid-ocean-ridge spreading center, and was then modified in a supra-subduction-zone (SSZ) environment (*e.g.*, Zhou *et al.*, 1996, 2005).

The Ray-Iz ophiolite is a block of ~400 km^2, set in a mélange belt sandwiched between sediments from the European continent and the eastern early Paleozoic arc complexes. From north to south, it comprises (1) a clinopyroxene-rich harzburgite or lherzolite zone, (2) a dunite-bearing harzburgite zone, which also contains economic chromitite deposits, and (3) a dunite–clinopyroxenite–gabbro complex (*e.g.*, Shmelev, 2011). A wide range of Neo-Proterozoic to Devonian ages has been reported for the ophiolite (*e.g.*, Batanova *et al.*, 2011). Previous studies have suggested that the clinopyroxene-rich harzburgite or lherzolite zone in the Ray-Iz ophiolite was generated at a mid-ocean ridge, and the dunite- and chromitite-bearing harzburgite zone in a forearc spreading region (*e.g.*, Batanova *et al.*, 2011; Shmelev, 2011).

2.2. *UHP*–SuR associations in the Tibet and Polar Urals ophiolites

The *UHP*–SuR mineral assemblages in the Luobusa ophiolite have been separated from, or observed *in situ*, in the high-Cr# chromitites and harzburgites from the dunite-facies zone and the Cpx-poor harzburgite zone, and have been studied over ~30 years (see references above). In the early studies, tons of chromitite, harzburgite and dunite were crushed for mineral separation, resulting in uncertainty about the relationships between individual *UHP*–SuR phases and with their host rocks, and raising the possibility of contamination during processing. In the last 10 years, *in situ* observations of *UHP*–SuR phases with clear spatial contexts with chromite, olivine, PGE alloys or Fe–Ti alloys have confirmed their natural origin (*e.g.*, Yang *et al.*, 2007, 2014; Dobrzhinetskaya *et al.*, 2009; Yamamoto *et al.*, 2009; Satsukawa *et al.*, 2015; Zhang *et al.*, 2016a).

Diamond has been the most controversial *UHP* mineral observed in the Luobusa ophiolite. It displays cubo-octahedral morphology and flat cubic facets, similar to synthetic diamonds but clearly different from kimberlite-borne diamonds (Fig. 2a; *e.g.*, Bai *et al.*, 1993; Robinson *et al.*, 2004; Yang *et al.*, 2014, 2015a and b). Inclusions of Ni–Mn–Co alloys and REE phases, trace-element patterns, N-isotope distributions and the observation of diamond *in situ* in chromitites suggest that these unusual diamonds crystallized rapidly in a natural, carbon-saturated, Ni–Mn–Co-rich melt under diamond-stability conditions (*e.g.*, Yang *et al.*, 2014, 2015a and b; Howell *et al.*, 2015; Griffin *et al.*, 2016a). Several diamonds have been found *in situ*, enclosed in a brecciated matrix of amorphous carbon within the chromitite (Fig. 2a; Yang *et al.*, 2014, 2015a and b). The second line of evidence for *UHP* conditions is the exsolution of diopside and coesite from chromite, suggesting inversion of a high-*P* polymorph with a Ca-ferrite (CF) structure (Yamamoto *et al.*, 2009; Zhang *et al.*, 2017), and the observation of fabrics inherited from wadsleyite + CF chromite of the Mantle Transition Zone (Satsukawa *et al.*, 2015). Other strong evidence includes blades of granular coesite (interpreted pseudomorphs after stishovite) intergrown with kyanite and amorphous silicates as a rim around a Fe–Ti alloy, and the TiO_2 II (αPbO_2 structure) and cubic BN enclosed within the coesite blades, implying very low fO_2 and derivation from minimum depths of ~300 km (Yang *et al.*, 2007; Dobrzhinetskaya *et al.*, 2009). The occurrence of Si-rich rutile ($(Ti_{0.82}Si_{0.18})O_2$; Yang *et al.*, 2003) and an octahedral Mg-silicate with an inverse-spinel structure (Robinson *et al.*, 2004; Griffin *et al.*, 2016a) also suggests a *UHP* origin.

The SuR phases (Table S1) from the Luobusa ophiolite include (1) SiC with inclusions of native Si and Fe-silicide (Fig. 2b; *e.g.*, Robinson *et al.*, 2004; Yang *et al.*, 2015b), (2) Fe- and W-carbides (*e.g.*, Robinson *et al.*, 2004), (3) Ti-bearing corundum with inclusions of Ti-bearing oxides, carbides, and nitrides (Fig. 2c; Xu *et al.*, 2013), and (4) balls of native Fe–FeO, native Cr and Ti (Fig. 2d; Yang *et al.*, 2008, 2015b; Liou *et al.*, 2014; Xu *et al.*, 2015). SiC has been observed *in situ* as inclusions in olivine and/or chromite of peridotite and chromitite (Liang *et al.*, 2014; Yang *et al.*, 2015b; Zhang *et al.*, 2016a). These phases and textural relationships suggest fO_2 conditions well below the IW buffer (Fig. 3) and temperatures of >1400–1500 °C (*e.g.*, Ulmer *et al.*, 1998; Griffin *et al.*, 2016a). The clear negative anomalies in Eu, Sm, Yb and Y relative to other trace elements in the Luobusa diamonds, and the lack of Fe inclusions or detectable Fe concentrations (Howell *et al.*, 2015), also suggest that the *UHP* diamonds crystallized in a reduced environment (at least below the IW buffer), where trivalent Eu, Sm, Yb, Y become divalent, and Fe is present as Fe metal (Fig. 3; Papike *et al.*, 2016).

In the Ray-Iz ophiolite, Yang *et al.* (2015a) have reported diamond and CF-type chromitite similar to those in the Luobusa ophiolite, and coesite in the diamond. The SuR phases are similar in nearly all respects to those from the Luobusa ophiolite (Table S1), suggesting that the two ophiolites may have experienced comparable tectonic processes and mantle-cycling dynamics.

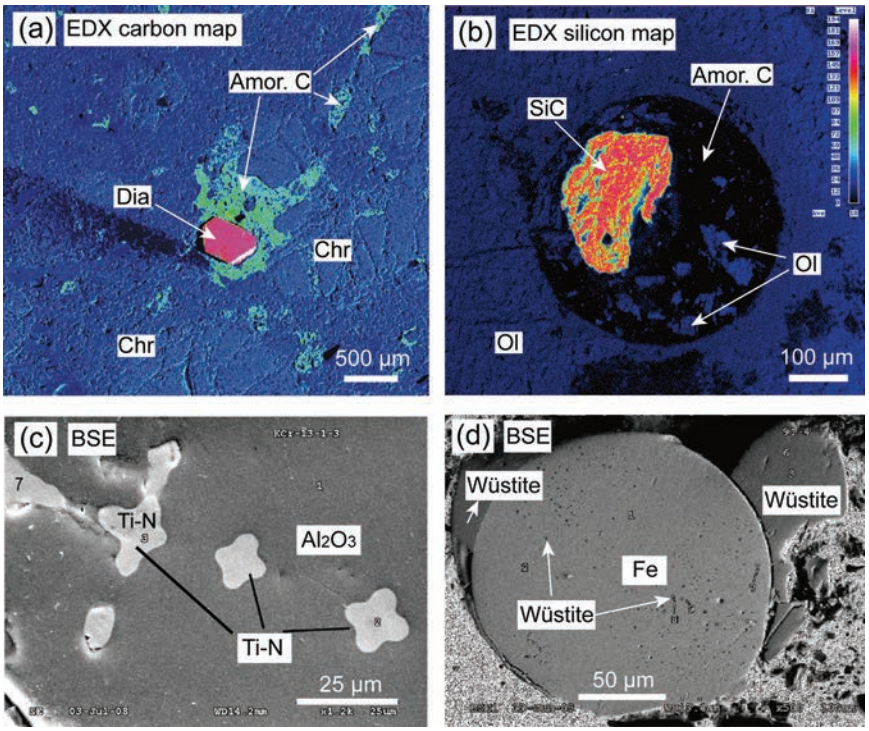

Fig. 2. Representative super-reduced minerals in the Tibet and Polar Urals ophiolites. (a) A diamond sitting in a matrix of amorphous carbon, observed *in situ* in a chromitite from the Ray-Iz ophiolite (energy-dispersive X-ray (EDX) map showing carbon distribution; reprinted from Yang *et al.* (2015a, Fig. 8d), with permission from Elsevier). (b) A SiC grain sitting in a ball of amorphous carbon which also contains brecciated olivine fragments, observed *in situ* in olivine of a Luobusa harzburgite (EDX map showing silicon distribution, reprinted from Yang *et al.* (2015b, Fig. 10c), with permission from the International Union of Geological Sciences Publications Committee). (c) Ti-bearing corundum including Ti-nitrides (back-scattered electron (BSE) image, reprinted from Xu *et al.* (2013, Fig. 5b), with permission from Executive Editor of *Acta Petrologica Sinica*). (d) A native Fe ball with drops of FeO (wüstite) inclusions and FeO rims, set in epoxy resin (BSE image, reprinted from Liou *et al.* (2014, Fig. 9F), with permission from Elsevier). Abbreviations: Dia, diamond; Amor. C, amorphous carbon; Chr, chromite; Ol, olivine.

2.3. Existing models for the genesis of *UHP*–SuR associations

Two basic models have been proposed to explain the genesis of the *UHP*–SuR association in the ophiolitic chromitites and peridotites. One proposes that the *UHP* and SuR phases were encapsulated in chromite grains that crystallized from high-Cr magmas, in the Mantle Transition Zone or the lower part of upper mantle, and then migrated upwards through a mantle plume (Yang *et al.*, 2007, 2014), or in upwelling mantle driven by the rollback and breakoff of a subducting slab (Zhou *et al.*, 2014; Zhang *et al.*, 2016a). The other model proposes that both the *UHP* chromitites and their enclosing peridotites originally formed at shallow depths, but were subducted into the Mantle Transition Zone, and later exhumed back to shallow depths (Arai, 2013). McGowan *et al.* (2015) and Griffin *et al.* (2016a) showed how slab rollback would develop a focused upwelling channel that would bring the harzburgite massifs and their chromitites to the surface on timescales of 6–10 m.y.

These models have treated the SuR phases as forming together with the *UHP* materials in the deep, reduced upper mantle or Mantle Transition Zone. However, most of the *UHP* phases do not require low fO_2 conditions, and only a few of the SuR phases require high P (see above and Table S1). Are the *UHP* and SuR phases necessarily related? Can other mechanisms introduce such low-fO_2 assemblages into the ophiolitic chromitites and peridotites? How could these SuR assemblages survive in the more oxidizing ophiolitic environment? These questions are still enigmatic. Here we use a remarkable, recently recognized mineral system from Mt Carmel, Israel, to suggest an alternative genesis for the ophiolitic SuR phases.

3. Mount Carmel, Israel: basalts, xenocrysts and SuR assemblages

3.1. Geological background and sampling

Cretaceous pyroclastic vents (volcanics) and related alluvial deposits in the Mt Carmel-Kishon River area of northern Israel (southern Galilee; Fig. S1 in Supplementary Material) have recently yielded abundant xenocrysts of corundum, moissanite, native Fe and a range of highly reduced phases (Griffin *et al.*, 2016b and c). This area lies within a complex system of faults, related to the Africa–Arabia plate boundary that evolved into the Dead Sea Transform, active since Miocene time. The early

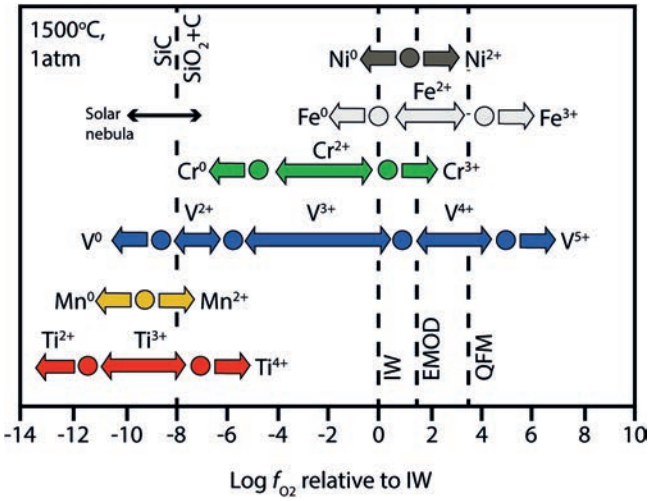

Fig. 3. Oxygen fugacity (fO_2) of relevant buffer pairs relative to IW at 1500 K, 1 atm. Modified from Papike *et al.* (2016). QFM, quartz–fayalite–magnetite buffer; EMOD, enstatite–magnesite–oxygen–diamond (or graphite) buffer; IW, iron–wüstite buffer; SiC stability defined by the two reactions discussed in the text (from Ulmer *et al.*, 1998).

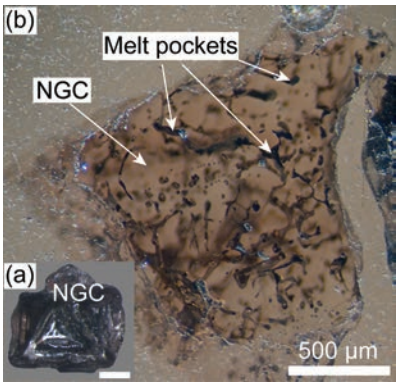

Fig. 4. (a) Single crystal of non-gem corundum (NGC, or "Carmel Sapphire"; inset in (b)) with hopper faces. White bar is 500 µm long. (b) Binocular-microscope photo of a corundum aggregate, with melt pockets (dark) visible as grain-boundary networks and internal bubbles (from Griffin *et al.*, 2016b).

development of the Jurassic–Early Cretaceous Levant magmatic province coincided with major rifting across Africa, but no major events of rifting (or subduction) are correlated with the sparse Early Cretaceous continental magmatism in Israel. This magmatism (137–139 Ma; *e.g.*, Segev, 2009) comprises subalkaline to alkaline basalts, nephelinites, and basanites with hotspot/mantle plume geochemical and isotopic signatures (Garfunkel, 1989; Stein & Hofmann, 1992, 1994; Laws & Wilson, 1997). The Cretaceous volcanics were covered by Eocene and younger formations, and were exposed by uplift and block-faulting, with subsequent erosion.

Late Cretaceous (94–98 Ma, Turonian-Cenomanian) volcanic activity in northern Israel took place in the Mt Carmel–Umm El Fahm area (Fig. S1). The dominant volcanic rocks are pyroclastics of mafic to ultramafic composition, erupted in a shallow marine environment (Sass, 1980). Black (fresh) pyroclastics occur in eruptive vents, whereas variegated pyroclastics occur as layers interbedded with carbonates. Lapilli consist both of volcanic glass (now cryptocrystalline) and microporphyritic mafic to ultramafic lavas. Analyses of the latter show that the magmas were tholeiitic picrites (Griffin *et al.*, 2016b). The pyroclastic deposits carry mantle-derived xenoliths and xenocrysts (spinel peridotites, garnet ± spinel pyroxenites, garnet websterites), crustal garnet–ilmenite granulites, and megacrystic Mg-ilmenite, amphibole and clinopyroxene; *P–T* estimates on garnet websterites suggest maximum conditions of *ca.* 2.3 GPa and 1030 °C (Esperanca & Garfunkel, 1986; Mittlefehldt, 1986; Apter, 2014; our unpublished data).

Over the last decade, the Shefa Yamim exploration project, focused on placer gem deposits, has recovered xenocrysts of corundum (sapphire, ruby and "non-gem" corundum) and moissanite (SiC). Aggregates of "non-gem corundum" ("Carmel Sapphire"; hereafter NGC) up to >24 cts in weight have been recovered. Crystals of moissanite can be over 4 mm long. Sampling of the Cretaceous pyroclastic rocks on Mt Carmel has yielded moissanite, all types of corundum, and the suite of minerals described below. The distribution of NGC in the drainage system suggests that it, and other minerals discussed here, are derived mainly from the Cretaceous pyroclastics. Analyses of rocks and minerals (with crystallographic data) are given by Griffin *et al.* (2016b and c); analytical methods are briefly described in the Supplementary Material.

3.2. Corundum and its growth history

Most xenocrysts of NGC are yellow-orange to dark brown (Fig. 4). Nearly all are irregular in shape, but some are rectangular prisms with depressed faces suggestive of hopper growth (Fig. 4a). Study of transparent fragments reveals intricate three-dimensional networks of darker material, which represent pockets of trapped melts (see below) and mineral inclusions (Fig. 4b). Some larger specimens are cut by veins consisting mainly of carbon, and one of the largest specimens studied is a breccia of corundum fragments in a matrix of such carbon (Fig. 5). Raman spectroscopy (Fig. S2) indicates that the carbon is amorphous (Robertson, 1986).

Most fragments of NGC show a remarkable CL response (Fig. 6), which appears to be controlled by the substitution of Ti in the corundum. Low concentrations of Ti yield a bright CL response, whereas higher concentration zones (up to 1 at%) show a darker response, and the highest contents (up to 2.5 at%) essentially quench the CL. The Ti contents increase linearly toward the melt pockets, and thus appear to be related to crystal growth rather than to diffusion of Ti from the melts into the corundum (Fig. S3).

The CL images (Fig. 6) reveal that most NGC xenocrysts are aggregates of corundum crystals. The distribution of melt pockets and the related dark CL show that the crystals are skeletal, with intricate, crystallographically controlled internal cavities and the hollow faces typical of hopper

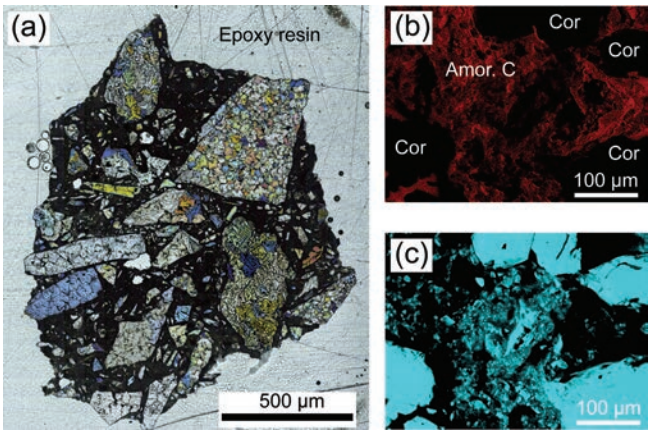

Fig. 5. (a) Thin section photo (plane polarized light) of fragments of corundum (Cor) aggregate cut by breccia veins with matrix of amorphous carbon (Amor. C). (b) Energy-dispersive X-ray map of a representative area of corundum grains and interstitial breccia veins showing the distribution of amorphous carbon (bright red). (c) X-ray map of the same area of (b) showing the distribution of aluminum (bright blue).

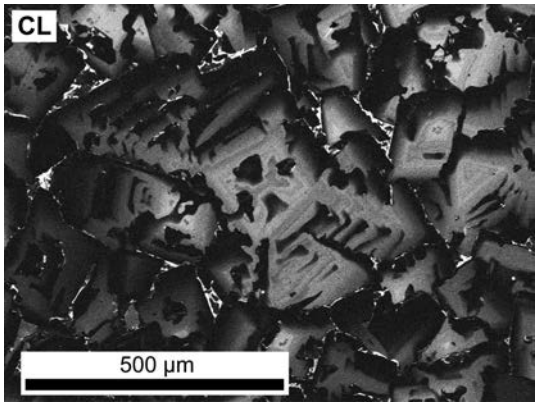

Fig. 6. Cathodoluminescence (CL) image of a representative corundum aggregate, showing growth zoning of individual crystals. Feathery dark areas indicate zones of highest Ti^{3+} content close to melt pockets trapped during growth.

growth (Fig. 6), which has provided a structure in which abundant melt pockets could be trapped. Electron backscatter diffraction (EBSD) mapping reveals that the aggregates consist of domains in which multiple individual crystals have very similar crystallographic orientation, while individual domains are misoriented to various degrees (Griffin *et al.*, 2016b). This clustering of similarly oriented crystals also is typical of hopper growth.

3.3. Melt pockets: mineral assemblages, melt compositions and quench structures

The melt pockets in the NGC can be divided into four types: Type S (silicate glass + oxides), Type A (alloy), Type N (nitrides + borides of Ti), and Type DF (SiO_2-free assemblages with fluorides). Types S, A and N appear to have been mutually immiscible during much of the corundum growth; they are found together in some melt

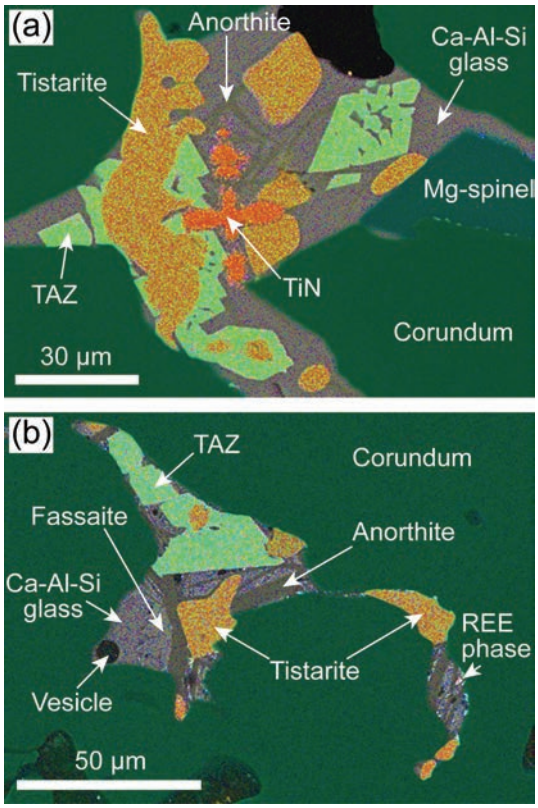

Fig. 7. Composite element map of S-type melt pockets (a, b) in corundum acquired by energy-dispersive X-ray spectroscopy–scanning electron microscopy. (a) Simple pocket with tistarite and "TAZ" oxides, in matrix of Ca–Al–Si glass containing quench blades of anorthite (dark brown), crosscut by TiN (red). (b) Similar to (a) but with large anorthite crystals overgrown by "fassaite"; note vesicle in the Ca–Al–Si glass. Light specks are REE phases.

pockets, or in separate pockets, which may be linked in three dimensions (Fig. 4b). They contain a remarkable array of crystalline phases, many requiring very low fO_2; more than half have not previously been reported as minerals, or are known only from meteorites (Table S2).

Type-S pockets (Fig. 7a, b) occur along grain boundaries, and in internal cavities. In these pockets, the most common crystalline phases are tistarite (Ti_2O_3), a new phase designated TAZ ($Ti_4Al_2ZrO_{11}$), and Mg–Ti–Al spinel $(Mg,Al,Ti)Al_2O_4$. The first two phases have been described by Griffin *et al.* (2016b); others (Table S2) will be described in detail as more complete datasets are accumulated. The crystalline phases in Type-S pockets are embedded in a fresh Ca–Al–Si oxide glass, with variable composition (Griffin *et al.*, 2016b). Electron microprobe analyses of the glass have totals averaging 97.5 wt%, suggesting the presence of dissolved unanalyzed volatiles in the glass; this is consistent with the presence of singe vesicles in some melt pockets. The glasses in the Type-S pockets contain percent levels of Ti, Zr and the light rare earth elements (LREE). They show an array of apparent quench and reaction structures, producing blades of anorthite, rhombs of "fassaite" (Fig. 7b), and needles of zirkelite and unidentified REE-phases in the glass matrix.

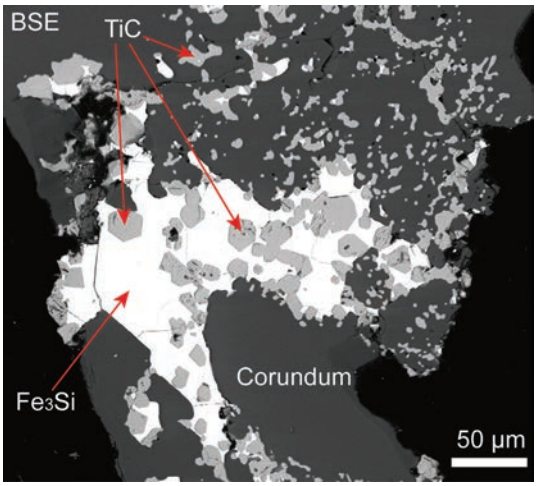

Fig. 8. Back-scattered electron (BSE) image of A-type melt pocket in corundum shows euhedral crystals of TiC in Fe_3Si. The pattern suggests that growing corundum crystals trapped the solid TiC, but pushed most of the Fe_3Si melt into the interstitial spaces, where it continued to crystallize TiC.

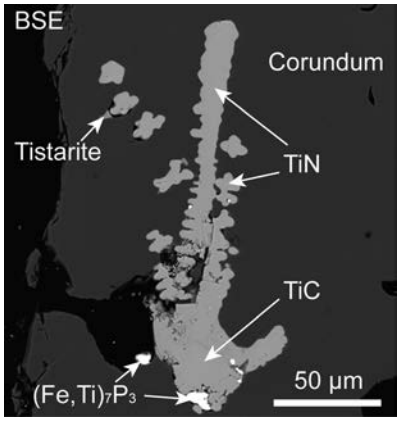

Fig. 9. BSE image of N-type melt pocket in corundum shows TiN lattices with phosphides and TiC of A-type melt.

Type-A pockets are found both along grain boundaries and within corundum crystals. The two most abundant phases are TiC (khamrabaevite) and Fe_3Si (gupeiite) (Fig. 8), but the pockets also contain a range of Fe–Ti–Si–P alloy phases (Table S2). In many cases these are intergrown in patterns that suggest the unmixing or crystallization of originally homogeneous alloy melts. The detailed characterization of these phases is in progress.

Type-N pockets comprise mainly osbornite (TiN) with variable stoichiometry, accompanied by minor silicides and Ti diboride (Griffin *et al.*, 2016b). They commonly show elongate forms with lobate boundaries; in some cases, these form rectangular networks (Fig. 9), suggesting that they were trapped in the internal cavities of skeletal corundum.

Type-DF pockets (Fig. 10) are represented mainly by angular grains of hibonite trapped between crystals of corundum; native V occurs as rounded grains together with hibonite ($CaAl_{12}O_{19}$) and grossite ($CaAl_4O_7$), in some cases ringed by fluorite. This assemblage is also found as coarse-grained microxenoliths consisting of hibonite,

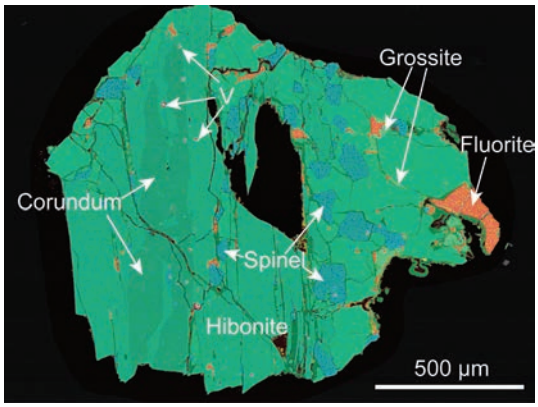

Fig. 10. Composite energy-dispersive X-ray element map of DF-type melt pocket in corundum, showing resorbed corundum with hibonite, native V, grossite, spinel, fluorite, and unknown Zr–Ti oxide.

grossite, Mg–V–Al spinel and fluorite; native V occurs as drops and balls scattered through the hibonite. Corroded laths of Ti-free corundum occur centrally in some laths of hibonite, evidence of the peritectic reaction corundum + liquid → hibonite.

3.4. "Fe balls", metal-oxide melts and wüstite

Both the vent pyroclastics and the associated alluvial deposits contain abundant spheres (up to 3 mm diameter) of native Fe and a range of Fe–Ti oxides. Some balls are pure native Fe; more rarely they are alloys of Fe with significant contents of Mn, Cr and Ni. These balls are commonly surrounded by rims of Fe–Ti oxides; similar oxide assemblages occur as individual spheres or aggregates of spheres (Fig. 11), many of which are vesicular or contain one large spherical central void. Three populations have been recognized in terms of bulk composition: (1) >80 wt% FeO, ≤10 wt% TiO_2; (2) mean FeO 50 wt%, TiO_2 30 wt%; (3) mean FeO 15 wt%, TiO_2 50 wt%. The first type, where crystalline, consists of dendritic wüstite (nearly stoichiometric FeO) crystals in a matrix richer in Si, Ca and Al. The more Ti-rich varieties commonly crystallize blades of armalcolite/pseudoferrobrookite ($FeTi_2O_5$; Bowles, 1988) in a matrix rich in Si, Ti, Ca and K. These balls appear to represent metal-oxide melts, immiscible with one another and with pure Fe melts. Individual aggregates of spheres may contain any combination of these types. Several of these balls are attached to fragments of corundum, providing a direct link between these two parts of the system. Wüstite also occurs in the form of angular, finely crystalline, vesicular fragments up to several mm across, commonly with minor (<1 at%) Mn and Si.

3.5. Moissanite

The Mt Carmel occurrences are notable for their abundance of SiC, which occurs as crystals up to 4.14 mm long; this is much larger than moissanite reported from kimberlites, ophiolites (typically ≤200 μm) or xenoliths (Di Pierro *et al.*,

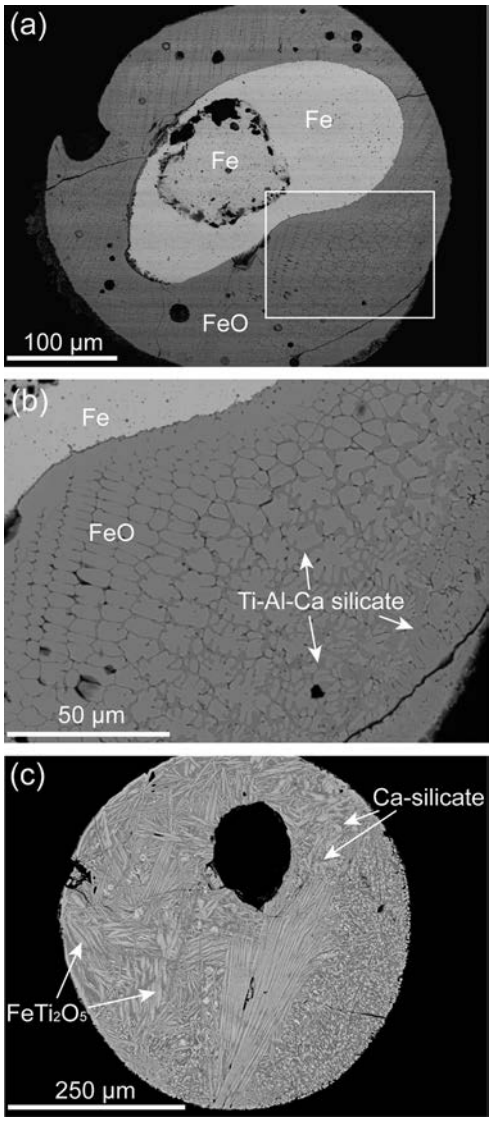

Fig. 11. BSE images of Fe and Fe–Ti oxide melts in spherical balls and aggregates from Mt Carmel volcanics. (a) Cored Fe ball with wüstite-dominated oxide–silicate melt shell. (b) Enlarged area of the white box in (a). (c) Quenched oxide-melt ball with Fe–Ti oxide (bright) and unknown Ca-bearing silicate phase (dark).

2003; Di Pierro & Gnos, 2016; Trumbull *et al.*, 2009; Shiryaev *et al.*, 2011; Liu *et al.*, 2015; Xu *et al.*, 2015). Moissanite has been observed together with TiC, $TiSi_2$ and other phases in two melt pockets in the NGC, providing a physical link between these highly reduced mineral assemblages. The occurrence of Ti–V alloys and Ca–Al–Fe silicides as inclusions in the Mt Carmel SiC links them to the Type-DF assemblage described above (Table S2), and distinguishes them from the moissanite from kimberlites (Shiryaev *et al.*, 2011) and ophiolites.

3.6. Carbon veins and brecciation

Some larger NGC fragments are breccias, with angular clasts of the NGC embedded in a matrix composed dominantly of amorphous carbon (Figs. 5, S2). It is mixed with finely dispersed corundum, various phases common in the melt pockets, SiC and Fe sulfides. Some samples contain abundant grains of cryolite (Na_3AlF_6) and an unnamed K–Al fluoride. Transmission electron microscope (TEM) images show that some corundum grains and melt pockets also are cut by parallel-sided veins of amorphous carbon, ranging from several tens of micrometers to $\leq$50 nm thick (Fig. S4). This observation, and the lack of detectable Cl (a component of epoxy resin), make it unlikely that the amorphous carbon is an artifact of sample preparation. The microstructures suggest brittle fracture, turbulent mixing and injection of carbon-rich fluids that also contained high levels of S and F; these processes may be linked to the explosive eruption of the host magma.

4. Discussion

4.1. *P–T–f*O_2 constraints

Perhaps the best constraint on *P* and *T* during corundum growth is provided by the occurrence of anorthite as a quench phase (Fig. 7), and more rarely as a euhedral phase, in the glass pockets. Anorthite melts congruently up to 9 kbar; at higher *P*, it melts incongruently to corundum + melt, and is unstable above 30 kbar (Goldsmith, 1980). The appearance of anorthite as a late phase in the residual melts is consistent with the peritectic reaction corundum + melt → anorthite; this suggests that most corundum crystallization occurred at 9–30 kbar (*ca.* 30–100 km depth) and ~1450–1550 °C.

Other constraints on *T* are broadly similar. The large spinel grains in the melt pockets commonly have excess Al_2O_3, consistent with high-*T* crystallization in the presence of corundum. The maximum Al_2O_3 in Ti-free spinels is 77.5 wt%, implying crystallization at ~1400 °C at 1 atm (Hallstedt, 1992). The peritectic reaction corundum + liquid → hibonite (Fig. 10) occurs at ~1790 °C in the $CaO–Al_2O_3$ system, but extends down to 1475 °C in the 1-atm $CaO–Al_2O_3–SiO_2$ system.

Gupeiite (Fe_3Si), a common phase in the Type-A melt pockets, crystallizes from reduced melts at 1200–1300 °C at 1 atm (Kubaschewski, 1982). Tistarite (Ti_2O_3) crystallizes from Ti–O melts at 1700–1870 °C, and Fe_2P from 1166–1370 °C in the binary system; FeTiSi is on the liquidus in the ternary system from ~1530°C to ~1200 °C (Weitzer *et al.*, 2008). Most of the experimental data come from the ceramics and metallurgy literature, and were obtained at low *P*; they probably give minimum *T* estimates. In addition, the presence of volatiles (C, N, F) may have lowered liquidus temperatures. However, it seems clear that the corundum, and the associated moissanite, crystallized at high (magmatic) *T*. The moissanite associated with these phases clearly is not a product of low-*T* processes, as argued by Schmidt *et al.* (2014).

The low *f*O_2 of the assemblages in the melt pockets is defined by the presence of SiC, Ti_2O_3, TiO and native V, and the abundance of reduced phases such as TiN and TiC, both with Ti^{2+} (our unpublished EELS data) and Fe_3Si. These assemblages indicate *f*O_2 between 8 and 11 log units

below the IW buffer (Fig. 3). The absence of Fe, Ni, Mn or Cr in the silicate and oxide phases in the melt pockets suggests that fO_2 was at least below the IW buffer, consistent with the removal of Fe as immiscible melts (Fig. 11) by the time the skeletal/hopper NGC aggregates began to grow.

4.2. Definition of process using the Mt Carmel example

While many aspects of the Mt Carmel volcanic system are not yet understood, the pyroclastic material does at least provide context at a grain (mm–cm) scale, allowing definition of parageneses and sequences. A simplified model of the processes involved has been constructed, linking the observations available at this time.

The growth of corundum as hopper or skeletal crystals implies rapid crystallization from a melt supersaturated in Al_2O_3; the regular arrangement of the crystals in the aggregates suggests growth on a substrate, rather than the random accumulation of phenocrysts from a magma. The quench structures in the melt pockets (Fig. 7) and the metal-oxide melts (Fig. 11) suggest that this process was part of an active magmatic/hydrothermal system that was terminated by the explosive eruption of the Cretaceous volcanic rocks. The key question becomes: how can Al-supersaturation, and the implied disequilibrium, be achieved in a magmatic system within the upper mantle (30–100 km depths)?

We suggest that such conditions might be imposed on magmas in conduits or magma chambers, and perhaps on the immediately adjacent mantle, if rising asthenosphere-derived magmas were accompanied by significant proportions of deep-mantle fluids. Numerous investigators (*e.g.*, Frost & McCammon, 2008; Rohrbach & Schmidt, 2011; Stagno *et al.*, 2013) have argued that the sublithospheric convective mantle (>250 km depth) is metal (Fe)-saturated; if this is correct, then any C–O–H fluids at these depths will be totally dominated by $CH_4 \pm H_2$ (*e.g.*, Zhang & Duan, 2009). The passage of such fluids through the more oxidized peridotitic mantle might be sustained by the reduction of the wall-rocks of fluid conduits, leading to removal of FeO, and/or the plating out of FeO-free phases on the walls of the conduit or magma chamber.

Interaction between such fluids and mafic–ultramafic magmas within a mantle plumbing system could lead to both very low fO_2 and supersaturation in Al_2O_3, through a linked reduction/desilication mechanism driven by reactions, such as:

$$SiO_2(\text{in silicate melt}) + CH_4 \rightarrow SiC + 2H_2O, \quad (1)$$

$$2CH_4 + 2H_2O \rightarrow 6H_2 + 2CO \rightarrow C + CO_2 + 6H_2, \quad (2)$$

$$CH_4 + CO_2 \rightarrow 2H_2 + 2CO \rightarrow C + CO_2 + 2H_2 \quad (\text{taking O out of silicates}). \quad (3)$$

Reactions (2) and (3) are well known from industrial-scale applications, in which the partial oxidation of methane is used to generate hydrogen and "syngas" (*e.g.*, Konnov *et al.*, 2004; Lemke *et al.*, 2005; Lyubovsky *et al.*, 2005).

The progressive reduction and desilication of a mafic–ultramafic magma, leading ultimately to the rapid precipitation of corundum from an Al_2O_3-supersaturated magma, can be accounted for by infiltration of $CH_4 \pm H_2$ fluids into a magma chamber (with initial $fO_2 \geq$ QFM), or in a magma-conduit situation.

In the first stage of the process, fO_2 in the magma is lowered to the magnetite–wüstite buffer (Fig. 3), leading to precipitation of the abundant, commonly vesicular, wüstite lapilli found in the ejecta. The CO_2 released by the reduction of magnetite would react with the magma to precipitate the observed aggregates of high-Mg dolomite, removing some Ca and Mg; this reaction can proceed only until fO_2 drops below the EMOD buffer (Fig. 3). It is noteworthy that the matrix of the SiC-rich xenolith described by Di Pierro *et al.* (2003; see below) consists of brucite, calcite and magnesite, which might represent low-T breakdown products of higher-T magmatic carbonates.

At this point the magma has been depleted in Fe, Ca and Mg, leading to enrichment in Si, Al and Ti. Once fO_2 reaches the IW buffer, most of the remaining Fe would be sequestered in metallic iron, alloy, or immiscible metal-oxide melts, represented by the abundant metallic spheres described above. With FeO (and other transition-metal oxides) removed from the magma, and a continued supply of $CH_4 \pm H_2$, the decline in fO_2 could accelerate to the point at which SiC becomes stable, through the reactions:

$$SiC + O_2 = C + SiO_2 \quad (\text{moissanite}-\text{carbon}-\text{quartz buffer}), \quad (4)$$

$$SiC + Mg_2SiO_4 + O_2 = C + 2MgSiO_3 \quad (\text{moissanite}-\text{olivine}-\text{carbon}-\text{pyroxene buffer}), \quad (5)$$

which define very similar fO_2 relative to the IW buffer (IW–8 at 1400–1500 °C; Fig. 3; Ulmer *et al.*, 1998).

The precipitation of SiC would lead to desilication of the magma; if rapid enough, this would drive the magma into supersaturation in Al_2O_3, as required for the rapid hopper/skeletal growth of the corundum (NGC) aggregates. The porous structure of the resulting crystal mass could allow for the passage of volatiles, while helping to isolate the precipitated phases from back-reaction with the magma. The hydrogen produced by the simplified reactions (2) and (3) is immiscible with water under mantle conditions (Bali *et al.*, 2013). Solution of the water in the remaining magma, and flushing of hydrogen through the crystal framework, could help drive down fO_2 within that framework still further, culminating in the precipitation of the highly reduced phases in the melt pockets. The

Type-DF and Type-N melts may represent the end-members of this fluid evolution, in terms of both desilication and lowering of fO_2, and the concentration of volatiles such as N, F and B.

Reactions (2) and (3) would precipitate abundant carbon, which may be represented in the carbon-rich veins and breccias. These reactions also produce CO_2 and H_2O, which could contribute to volatile overpressure, and thus to explosive eruption, fragmenting and ejecting the crystallized material that grew in the magma chamber or along the walls of the magma conduits.

This scenario is clearly speculative at this stage of the research, but provides several hypotheses that can be tested. The next stage will require the detailed mapping of the different types of mineral assemblages and their 3*D* and 4*D* relationships, the characterization of the large number of previously unrecognized phases, and stable-isotope data to constrain the sources of the fluids.

4.3. Other examples of moissanite, diamond and native metal occurrence

Moissanite is generally regarded as rare in nature, but it may be more abundant than commonly realized. It has been separated from kimberlites and lamproites (Shiryaev *et al.*, 2011) and from kimberlite-borne eclogite xenoliths (our unpublished data), and reported as inclusions in diamonds (*e.g.*, Moore & Gurney, 1989; Leung *et al.*, 1990). A summary of the literature is provided by Di Pierro & Gnos (2016).

Prior to the Mt Carmel discoveries, the largest natural crystals of moissanite (1–2 mm) were reported from a beach cobble found in Turkey (Di Pierro *et al.*, 2003; Di Pierro & Gnos, 2016). The source of the cobble is not known, but it is believed to come from Tertiary volcanics in the region. The moissanite occurs together with *ca.* 25 vol% of SiO_2, with minor phlogopite and pyroxene, in a fine-grained matrix of brucite, magnesite and calcite. Moissanite crystals contain inclusions of native Si, Fe-silicides and Ca–Al–Si phases, some rich in REE, which the authors interpret as formed by the partial decomposition of high-*P* phases.

The recent (from 2012) explosive eruptions of the Tolbachik fissure on the Kamchatka peninsula produced mafic pumice carrying abundant microdiamonds, similar in morphology and C-isotope composition to the Tibetan diamonds (Gordeev *et al.*, 2014; Karpov *et al.*, 2014). The diamonds are associated with moissanite, Ti-rich corundum, and "iron oxide globules", providing a possible link to the Mt Carmel association. Native metals (Fe, Cu and Au) have crystallized in pumice vesicles, suggesting that the gases exsolved from the melt created a fO_2 at or below the IW buffer. Karpov *et al.* (2014) noted that similar associations of native metals and SiC are frequently found in the effusive products of volcanoes along the Kuril-Kamchatka volcanic arc, and Kaminsky *et al.* (2016) cataloged occurrences of diamond in Kamchatka lavas and dykes.

The Avacha volcano in Kamchatka carries polycrystalline microdiamond with dispersed SiC (Gorshkov *et al.*, 1995; Kaminsky *et al.*, 2016). These diamond aggregates contain inclusions of Mn–Ni–Fe-silicides and W and B carbides, indicating a very reduced environment. Gorshkov *et al.* (1995) argue that the diamond grew on a fine-grained matrix of SiC, through the reaction of Si or quartz with "carbon-bearing magmatic gases". Kaminsky *et al.* (2016) prefer a substrate of metal carbides and silicides, with SiC and Si appearing at a late stage in the evolution of the diamond aggregates, in a low-*P* environment analogous to diamond production by chemical vapor deposition.

Spinel-peridotite xenoliths from the same volcano contain native Fe and Ni, and Fe silicides (Ishimaru *et al.*, 2009) indicative of a local reducing environment in the sub-arc mantle. The reduced phases are small and clearly out of equilibrium with their relatively oxidized host, and even with one another. The authors interpret this disequilibrium, and microstructural evidence, as showing that the reduced phases were deposited through interaction between the host and highly reduced C–H fluids injected shortly before eruption. They also note that the native Fe is free of Ni, which is the case in both the ophiolitic peridotites and chromitites, and most of the Mt Carmel "Fe balls".

4.4. Similarities and differences

Some key similarities and differences in the phase associations reported from the localities are obvious in Table S1. The most striking *difference* is that no *UHP* phases have been recognized in the Mt Carmel samples; this is consistent with the presence of anorthite in the Type-S melt pockets, since crystallization of anorthite is limited to depths $\leq\sim$100 km (Goldsmith, 1980).

The most striking *similarities* are in the presence of high-*T* SuR phases, notably moissanite with metallic melt inclusions (Fe-silicides), in all four localities. This is accompanied in each instance by Ti-rich corundum, a key feature of the Mt Carmel association. TiC (khamrabaevite), TiN (osbornite) and possibly the TAZ phase are reported as inclusions in Ti-rich corundum from both the Tibetan and Polar-Urals localities, as well as the Mt Carmel samples. Ti-rich corundum is also reported from the Tolbachik lavas (Karpov *et al.*, 2014), but the inclusion data are not yet available. Ishimaru *et al.* (2009) report "possible native Ti" in an Avacha xenolith, but the analytical sum is 72.5 wt%, suggesting that this phase may be TiC. Tistarite has not been recognized from Kamchatka, nor from the Tibetan or Uralian localities. However, Xu *et al.* (2013) give analyses of "TiO_2" inclusions in corundum, with levels of MgO and other minor elements similar to those seen in the Mt Carmel (and Allende) tistarite (Griffin *et al.*, 2016b). Since oxygen apparently was not analyzed separately by Xu *et al.* (2013), these analyses may in fact represent tistarite.

The Fe balls with wüstite rims described from Tibet and the Polar Urals (Fig. 2d) are similar in structure to those seen in the Mt Carmel samples, although the oxide rims on

Fe balls at Mt Carmel apparently represent more complex oxide melts, rather than simply wüstite (Fig. 11). Fe-oxide balls are reported from the Tolbachik volcano, but there are only surface analyses and no information is available on the internal structure.

Breccia veins with amorphous carbon host the *in situ* diamonds and SiC reported from Tibet and the Polar Urals (Fig. 2a, b; Yang *et al.*, 2014, 2015a and b). Such breccia veins are common in the Mt Carmel corundum aggregates (Fig. 5), and polycrystalline microdiamond with amorphous carbon is reported from Avacha (Kaminsky *et al.*, 2016). Carbon appears to have played an important role in the development of the SuR associations in all four localities.

However, the carbides of Fe and W, and the native Ni, Co and PGEs, found in the chromitites and peridotites of both Tibet and the Polar Urals, and the volcanic rocks of Kamchatka (cohenite, $(Fe,Ni,Co)_3C$; Gordeev *et al.*, 2014) are not recognized in the Mt Carmel material. This may reflect a key difference in their respective situations: in the former localities, the reducing fluids appear to have interacted with wall-rock peridotites, as well as with the more evolved mafic melts proposed for the Mt Carmel system.

One common factor among these various localities is the presence of deep-seated mantle rocks or volcanism, related either to deep subduction and slab rollback (Kamchatka, Tibet, Polar Urals), or to the rise of "hot-spot" magmas (Mt Carmel; Stein & Hofmann, 1992, 1994). Another, related commonality is their tectonic setting on plate boundaries (Pacific subduction, continental-collision zones; the Dead Sea Transform). These major translithospheric structures provide the channels along which deep-seated rocks, magmas and deep-mantle fluids ($CH_4 \pm H_2$) may rise and mix. If this is the case, further investigation of the trace minerals carried by explosive magmas in such situations should turn up evidence that such processes are more widespread than currently recognized.

4.5. Introduction of SuR phases into ophiolites: a speculative model

Based on the inspiration of the Mt Carmel example, we speculate that the SuR phases observed in the Tibetan and Polar-Urals ophiolites probably did not experience a long residence time in the convective upper mantle or the Mantle Transition Zone, although some *UHP* materials may have done so. The un-aggregated nitrogen in the Tibetan ophiolitic diamonds (Howell *et al.*, 2015; Yang *et al.*, 2015b), the coexistence of SiC and FeO-bearing olivine and chromite (*e.g.*, Zhang *et al.*, 2016a), the intergrowth of nitrides, native Fe and Ti with oxides and silicates in a reaction rim around a partially unmixed Fe–Ti alloy (Yang *et al.*, 2007; Dobrzhinetskaya *et al.*, 2009), and the transition-metal alloys with complex unmixing textures (Xu *et al.*, 2015; Yang *et al.*, 2015a and b; Fig. 2d), all suggest that these phases were produced and then quenched during a rapid dynamic process, which could freeze-in the disequilibrium assemblages and textures and isolate them from the ambient convective mantle.

These features are consistent with the exhumation model described by McGowan *et al.* (2015) and Griffin *et al.* (2016a), in which the *UHP* chromitites and peridotites were brought to the surface in a focused upwelling channel, rooted in the Mantle Transition Zone and induced by slab rollback. Continuous influx of reduced C–H–O fluids ($CH_4 \pm H_2$) buffered by the metal-saturated convective mantle (Rohrbach & Schmidt, 2011) could react with chromitites and peridotites and drive down the local fO_2 to at least the IW buffer. The formation of SuR phases could begin deep in the convective mantle (Dobrzhinetskaya *et al.*, 2009), continue through the diamond-stability field (Howell *et al.*, 2015), and climax with ascent into the shallow lithosphere. The short time scale for the exhumation of the deep-seated chromitites and peridotites is supported by numerical modeling, which shows an ascent time of less than a few million years from the Mantle Transition Zone to the lithosphere (McGowan *et al.*, 2015; Griffin *et al.*, 2016a). The implied rapid cooling at shallow depths would facilitate the preservation of SuR–*UHP* associations in the shallow lithospheric mantle.

The interaction of $CH_4 \pm H_2$ fluids with the solid phases of the chromitites and peridotites during ascent can account for the coexistence of some *UHP* and SuR phases in the ophiolites. It can explain the *differences* between the Tibet and Israel suites, but does not obviously account for their *similarities*; specifically, the association of Ti-rich corundum, related SuR phases and SiC were preserved both in the Mt Carmel and the ophiolitic samples. To complete this story, it is required that the same types of fluids ($CH_4 \pm H_2$ from the deep convective mantle) interact with mafic magmas under relatively low-*P* conditions, leading to desilication, reduction, supersaturation in Al_2O_3, and the final production of SiC and amorphous carbon. These melts might have been generated by decompression melting in the asthenospheric component of the upwelling channel, and migrated upwards with the exhumation of buoyant harzburgites (including chromitites). A Mt Carmel-type evolution could then generate and emplace the main suite of SuR phases into the recycled chromitites and harzburgites, which subsequently accreted as part of the new oceanic lithosphere and eventually became the ophiolites in the Tibetan and Polar-Urals collision zones.

The analogies to the Kamchatka volcanism described above offer another possibility: the derivation of $CH_4 \pm H_2$ fluids from the subducting slab (*e.g.*, Ishimaru *et al.*, 2009), as rollback initiated the ascent of the harzburgites and chromitites in Tibet and the Polar Urals. Analyses of fluid inclusions in mantle-wedge peridotites (*e.g.*, Song *et al.*, 2009) have been ascribed to this mechanism. The serpentinization of slab and mantle-wedge peridotites could also supply $CH_4 \pm H_2$ fluids to the recycled

chromitites and harzburgites at shallow depths, and facilitate the formation and stability of SuR phases in the protoliths of the Tibetan and Polar-Urals ophiolites.

5. Conclusions

The low-P (<3 GPa) assemblage of SuR phases found as xenocrysts in Cretaceous volcanic rocks on Mt Carmel, Israel provides unique insights into the development of localized highly reduced volumes in the uppermost mantle. The mineral system is interpreted to reflect the interaction of mantle-derived $CH_4 \pm H_2$ fluids with the associated hot-spot basaltic magmas. These interactions led to desilication of the magma, supersaturation in Al_2O_3 with rapid growth of abundant Ti-rich corundum, and phase assemblages requiring fO_2 as low as IW-11. There are strong similarities between this system and the SuR phases and associated Ti-rich corundum in ophiolitic peridotites and chromitites in Tibet and the Polar Urals, and with less well-known SiC–diamond–corundum assemblages in volcanoes on the Kamchatka peninsula. We suggest that the ophiolitic SuR mineral suites probably reflect interaction between $CH_4 \pm H_2$ fluids and previously subducted peridotites (including chromitites) during their exhumation from the deep upper mantle or Mantle Transition Zone, overprinted by a shallow magmatic system similar to that observed at Mt Carmel. While the Tibet and Polar-Urals occurrences and those on Kamchatka involve large-scale deep subduction systems, there is no evidence of subduction associated with the Mt Carmel volcanics. The common factor among these occurrences appears to be the presence of $CH_4 \pm H_2$ fluids. We suggest that this type of fluids may commonly accompany deep-seated volcanism or magmatism, especially near plate boundaries and other lithosphere-scale discontinuities, and that SuR conditions may be more common than generally considered (though local and probably transient) in the upper mantle. This flux of $CH_4 \pm H_2$ fluids represents a previously unrecognized aspect of the global carbon cycle.

Acknowledgements: We thank Steve Craven and Manal Bebbington for help with difficult sample preparations, Will Powell for guidance with LAM-ICPMS analysis, Laure Martin (UWA) and Xian-Hua Li (IGG-CAS, Beijing) for isotopic analyses by SIMS, Martin Saunders with the TEM images, and Shi-Lin Li for preparation of Fig. 1 in this manuscript. We also thank Brian Marker (Chairman of the IUGS Publications Committee) and Hui Chen (Executive Editor of *Acta Petrologica Sinica*) for their permission to reprint Fig. 2b and c, respectively. Dorrit Jacob and Steven Foley contributed insightful discussions about oxygen fugacity and mineral growth. This study used instrumentation funded by ARC LIEF and DEST Systemic Infrastructure Grants, Macquarie University and industry. This is contribution 968 from the ARC Centre of Excellence for Core to Crust Fluid Systems (www.ccfs.mq.edu.au) and 1153 from the GEMOC Key Centre (www.gemoc.mq.edu.au).

References

Apter, D. (2014): High pressure indicator minerals from the Rakefet Magmatic Complex (RMC), Mt. Carmel, Israel. *in* "Proceedings of the GSSA Kimberley Diamond Symposium", Extended Abstract.

Arai, S. (2013): Conversion of low-pressure chromitites to ultrahigh-pressure chromitites by deep recycling: a good inference. *Earth Planet. Sci. Lett.*, **379**, 81–87.

Bai, W.J., Zhou, M.F., Robinson, P. (1993): Possibly diamond-bearing mantle peridotites and podiform chromitites in the Luobusa and Dongqiao ophiolites, Tibet. *Can. J. Earth Sci.*, **30**, 1650–1659.

Bali, E., Audetat, A., Keppler, H. (2013): Water and hydrogen are immiscible in Earth's mantle. *Nature*, **495**, 220–223.

Batanova, V.G., Belousov, I.A., Savelleva, G.N., Sobolev, A.V. (2011): Consequences of channelized and diffuse melt transport in supra-subduction zone mantle: evidence from the Voykar ophiolite (Polar Urals). *J. Petrol.*, **52**, 2483–2521.

Bodinier, J.L. & Godard, M. (2014): Orogenic, ophiolitic, and abyssal peridotites. *in* "Treatise on Geochemistry, 2nd edition", H.D. Holland & K.K. Turekian, eds., Elsevier, vol. 3, 103–167.

Bowles, J.F.W. (1988): Definition and range of composition of naturally occurring minerals with the pseudobrookite structure. *Am. Mineral.*, **73**, 1377–1383.

Chan, G.H.N., Aitchison, J.C., Crowley, Q.G., Horstwood, M.S.A., Searle, M.P., Parrish, R.R., Chan, J.S.L. (2015): U–Pb zircon ages for Yarlung Tsangpo suture zone ophiolites, south-western Tibet and their tectonic implications. *Gondwana Res.*, **27**, 719–732.

Chemenda, A., Matte, P., Sokolov, V. (1997): A model of Paleozoic obduction and exhumation of high-pressure/low-temperature rocks in the southern Urals. *Tectonophysics*, **276**, 217–227.

Di Pierro, S. & Gnos, E. (2016): Ca–Al–silicate inclusions in natural moissanite (SiC). *Am. Mineral.*, **101**, 71–81.

Di Pierro, S., Gnos, E., Grobety, B.H., Armbruster, T., Bernasconi, S.M., Ulmer, P. (2003): Rock-forming moissanite (natural silicon carbide). *Am. Mineral.*, **88**, 1817–1821.

Dobrzhinetskaya, L.F., Wirth, R., Yang, J.S., Hutcheon, I.D., Weber, P.K., Green II, H.W. (2009): High-pressure highly reduced nitrides and oxides from chromitite of a Tibetan ophiolite. *Proc. Natl. Acad. Sci. U. S. A.*, **106**, 19233–19238.

Dobrzhinetskaya, L.F., Wirth, R., Yang, J.S., Green, H.W., Hutcheon, I.D., Weber, P.K., Grew, E.S. (2014): Qingsongite, natural cubic boron nitride: the first boron mineral from the Earth's mantle. *Am. Mineral.*, **99**, 764–772.

Esperanca, S. & Garfunkel, Z. (1986): Ultramafic xenoliths from the Mt Carmel area (Karem Maharal volcano), Israel. *Lithos*, **19**, 43–49.

Frost, D.J. & McCammon, C.A. (2008): The redox state of Earth's mantle. *Annu. Rev. Earth Planet. Sci.*, **36**, 389–420.

Garfunkel, Z. (1989): Tectonic setting of Phanerozoic magmatism in Israel. *Isr. J. Earth Sci.*, **38**, 51–74.

Goldsmith, J.R. (1980): The melting and breakdown reactions of anorthite at high pressures and temperatures. *Am. Mineral.*, **65**, 272–284.

Golubkova, A., Schmidt, M.W., Connolly, J.A.D. (2016): Ultra-reducing conditions in average mantle peridotites and in podiform chromitites: a thermodynamic model for moissanite (SiC) formation. *Contrib. Mineral. Petrol.*, **171**, 41, doi:10.1007/s00410-016-1253-9.

Gordeev, E.I., Droznin, V.A., Dubrovskaya, I.K., Dvigalo, V.N. Maguskin, M.A., Muravyev, Ta.D., Titkov, N.V., Volynets, A.O. (2014): Fissure eruption on Tolbachik Dol (FTE-50), Kamchatka 2012–2013. *in* "8th Biennial Workshop on Japan-Kamchatka-Slaska Subduction Processes", Sapporo, Japan, 2 p.

Gorshkov, A., Seliverstov, V.A., Baikov, A.I., Anikin, L.P., Sivtsov, A. V., Duninbarkvskii, R.L. (1995): Crystallochemistry and genesis of carbonado from the melanocratic basaltoids of the Avacha volcano, Kamchatka Peninsula. *Geol. Ore Depos.*, **37**, 44–55.

Griffin, W.L., Afonso, J.C., Belousova, E.A., Gain, S.E., Gong, X.-H., González-Jiménez, J.M., Howell, D., Huang, J.-X., McGowan, N., Pearson, N.J., Satsukawa, T., Shi, R., Williams, P., Xiong, Q., Yang, J.-S., Zhang, M., O'Reilly, S.Y. (2016a): Mantle recycling: transition-zone metamorphism of Tibetan ophiolitic peridotites and its tectonic implications. *J. Petrol.*, **57**, 655–684.

Griffin, W.L., Gain, S.E.M., Adams, D.T., Huang, J.X., Saunders, M., Toledo, V., Pearson, N.J., O'Reilly, S.Y. (2016b): First terrestrial occurrence of tistarite (Ti_2O_3) ultra-low oxygen fugacity in the upper mantle beneath Mount Carmel, Israel. *Geology*, **44**, 815–818.

Griffin, W.L., Gain, S.E.M., Adams, D.T., Toledo, V., Pearson, N.J., O'Reilly, S.Y. (2016c): Deep-Earth methane and mantle dynamics: insights from northern Israel, southern Tibet and Kamachatka. *J. Proc. R. Soc. N. S. W.*, **149**, 17–33.

Hallstedt, B. (1992): Thermodynamic assessment of the system $MgO–Al_2O_3$. *J. Am. Ceram. Soc.*, **75**, 1497–1507.

Hébert, R., Bézard, R., Guilmette, C., Dostal, J., Wang, C.S., Liu, Z. F. (2012): The Indus-Yarlung Zangbo ophiolites from Nanga Parbat to Namche Barwa syntaxes, southern Tibet: first synthesis of petrology, geochemistry, and geochronology with incidences on geodynamic reconstructions of Neo-Tethys. *Gondwana Res.*, **22**, 377–397.

Howell, D., Griffin, W.L., Yang, J., Gain, S., Stern, R.A., Huang, J.-X., Jacob, D.E., Xu, X., Stokes, A.J., O'Reilly, S.Y., Pearson, N.J. (2015): Diamonds in ophiolites: contamination or a new diamond growth environment? *Earth Planet. Sci. Lett.*, **430**, 284–295.

Ishimaru, S., Arai, S., Shukuno, H. (2009): Metal-saturated peridotite in the mantle wedge inferred from metal-bearing peridotite xenoliths from Avacha volcano, Kamchatka. *Earth Planet. Sci. Lett.*, **284**, 352–360.

Kaminsky, F.V., Wirth, R., Anikin, L.P., Morales, L., Schreiber, A. (2016): Carbonado-like diamond from the Avacha active volcano in Kamchatka, Russia.*Lithos*, **265**, 222–236.

Karpov, G.A., Silaev, V.I., Anikin, L.P., Rakin, V.I., Vasil'ev, E.A., Filatov, S.K., Petrovskii, V.A., Flerov, G.B. (2014): Diamonds and accessory minerals in products of the 2012–2013 Tolbachik fissure eruption. *J. Volcanol. Seismol.*, **8**, 323–339.

Konnov, A.A., Zhu, J.N., Bromly, J.H., Zhang, D.K. (2004): Noncatalytic partial oxidation of methane into syngas over a wide temperature range. *Combust. Sci. Technol.*, **176**, 1093–1116.

Kubaschewski, O. (1982): Iron-Binary Phase Diagrams. Springer-Verlag, Berlin, 186 p.

Laws, E.D. & Wilson, M. (1997): Tectonics and magmatism associated with Mesozoic passive continental margin development in the Middle East. *J. Geol. Soc.*, **154**, 459–464.

Lemke, B., Roodhouse, C., Glumac, N., Krier, H. (2005): Hydrogen synthesis via combustion of fuel-rich natural gas/air mixtures at elevated pressure. *Int. J. Hydrogen Energy*, **30**, 893–902.

Leung, I., Guo, W.X., Fridman, I., Gleason, J. (1990): Natural occurrence of silicon carbide in a diamondiferous kimberlite from Fuxian. *Nature*, **346**, 352–354.

Liang, F.H., Xu, Z.Q., Zhao, J.N. (2014): In-situ moissanite in dunite: deep mantle origin of mantle peridotite in Luobusa ophiolite, Tibet. *Acta Geol. Sin.*, **88**, 517–529.

Liou, J.G., Tsujimori, T., Yang, J.S., Zhang, R.Y., Ernst, W.G. (2014): Recycling of crustal materials through study of ultrahigh-pressure minerals in collisional orogens, ophiolites, and mantle xenoliths: a review. *J. Asian Earth Sci.*, **96**, 386–420.

Liu, Y.S., He, D.T., Gao, C.G., Foley, S., Hu, Z.C., Zong, K.Q., Chen, H.H. (2015): First direct evidence of sedimentary carbonate recycling in subduction-related xenoliths. *Sci. Rep.*, **5**, 11547.

Luth, R.W. & Stachel, T. (2014): The buffering capacity of lithospheric mantle: implications for diamond formation. *Contrib. Mineral. Petrol.*, **168**, 1083, doi:10.1007/s00410-014-1083-6.

Lyubovsky, M., Roychoudhury, S., LaPierre, R. (2005): Catalytic partial "oxidation of methane to syngas" at elevated pressures. *Catal. Lett.*, **99**, 113–117.

McGowan, N.M., Griffin, W.L., Gonzalez-Jimenez, J.M., Belousova, E., Afonso, J.C., Shi, R.D., McCammon, C.A., Pearson, N. J., O'Reilly, S.Y. (2015): Tibetan chromitites: excavating the slab graveyard. *Geology*, **43**, 179–182.

Mittlefehldt, D.W. (1986): Petrology of high pressure clinopyroxenite series xenoliths, Mount Carmel, Israel. *Contrib. Mineral. Petrol.*, **94**, 245–252.

Moore, R.O. & Gurney, J.J. (1989): Mineral inclusions in diamond from the Monastery kimberlite, South Africa. *in* "Kimberlites and Related Rocks", J. Ross, A.L. Jaques, J. Ferguson, D.H. Green, S.Y. O'Reilly, R.V. Danchin, A.J.A. Janse, eds. Blackwell Scientific, Cambridge, England, vol. 2, 966–989.

Papike, J.J., Simon, S.B., Burger, P.V., Bell, A.S., Shearer, C.K., Karner, J.M. (2016): Chromium, vanadium, and titanium valence systematics in solar system pyroxene as a recorder of oxygen fugacity, planetary provenance, and processes. *Am. Mineral.*, **101**, 907–918.

Robertson, J. (1986): Amorphous carbon. *Adv. Phys.*, **35**, 317–374.

Robinson, P.T., Bai, W.J., Malpas, J., Yang, J.S., Zhou, M.F., Fang, Q.S., Hu, X.F., Cameron, S., Staudigel, H. (2004): Ultra-high pressure minerals in the Luobusa Ophiolite, Tibet, and their tectonic implications. *in* "Aspects of the Tectonic Evolution of China", J. Malpas et al., eds. *Geol. Soc. London Spec. Publ.*, **226**, 247–271.

Rohrbach, A. & Schmidt, M.W. (2011): Redox freezing and melting in the Earth's deep mantle resulting from carbon-iron redox coupling. *Nature*, **472**, 209–212.

Sass, E. (1980): Late Cretaceous volcanism in Mount Carmel, *Israel. Isr. J. Earth Sci.*, **29**, 8–24.

Satsukawa, T., Griffin, W.L., Piazolo, S., O'Reilly, S.Y. (2015): Messengers from the deep: fossil wadsleyite-chromite microstructures from the Mantle Transition Zone. *Sci. Rep.*, **5**, 16484, doi:10.1038/srep16484.

Schmidt, M.W., Gao, C., Golubkova, A., Rohrbach, A., Connolly, J.A.D. (2014): Natural moissanite (SiC) – a low temperature mineral formed from highly fractionated ultra-reducing COH fluids. *Prog. Earth Planet. Sci.*, **1**, 27.

Segev, A. (2009): $^{40}Ar/^{39}Ar$ and K–Ar geochronology of Berriasian-Hauterivian and Cenomanian tectonomagmatic events in northern Israel: implications for regional stratigraphy. *Cretaceous Res.*, **30**, 810–828.

Shiryaev, A.A., Griffin, W.L., Stoyanov, E. (2011): Moissanite (SiC) from kimberlites: polytypes, trace elements, inclusions and speculations on origin. *Lithos*, **122**, 152–164.

Shmelev, V.R. (2011): Mantle ultrabasites of ophiolite complexes in the Polar Urals: petrogenesis and geodynamic environments. *Petrology*, **19**, 618–640.

Song, S.G., Su, L., Niu, Y.L., Lai, Y., Zhang, L.F. (2009): CH_4 inclusions in orogenic harzburgite: evidence for reduced slab fluids and implications for redox melting in mantle wedge. *Geochim. Cosmochim. Acta*, **73**, 1737–1754.

Stagno, V., Ojwant, D.O., McCammon, C.A., Frost, D.J. (2013): The oxidation state of the mantle and the extraction of carbon from Earth's interior. *Nature*, **493**, 84–88.

Stein, M. & Hofmann, A.W. (1992): Fossil plume head beneath the Arabian lithosphere? *Earth Planet. Sci. Lett.*, **114**, 193–209.

—, — (1994): Mantle plumes and episodic crustal growth. *Nature*, **372**, 63–68.

Trumbull, R.B., Yang, J.S., Robinson, P.T., Di Pierro, S., Vennemann, T., Wiedenbeck, M. (2009): The carbon isotope composition of natural SiC (moissanite) from the Earth's mantle: new discoveries from ophiolites. *Lithos*, **113**, 612–620.

Ulmer, G.C., Grandstaff, D.E., Woerman E., Gobbels, M., Schonitz, M., Woodland, A.B. (1998): The redox stability of moissanite (SiC) compared with metal-metal oxide buffers at 1773 K and at pressures up to 90 kbar. *N. Jahrb. Mineral. Abh.*, **172**, 279–307.

Weitzer, F., Schuster, J.C., Naka, M., Stein, F., Palm, M. (2008): On the reaction scheme and liquidus surface in the ternary system Fe–Si–Ti. *Intermetallics*, **16**, 273–282.

Xu, X.Z., Yang, J.S., Guo, G.L., Xiong, F.H. (2013): Mineral inclusions in corundum from chromitites in the Kangjinla chromite deposit, Tibet. *Acta Petrol. Sin.*, **29**, 1867–1877 (in Chinese with English abstract).

Xu, X., Yang, J., Robinson, P.T., Xiong, F., Ba, D., Guo, G. (2015): Origin of ultrahigh pressure and highly reduced minerals in podiform chromitites and associated mantle peridotites of the Luobusa ophiolite, Tibet. *Gondwana Res.*, **27**, 686–700.

Yamamoto, S., Komiya, T., Hirose, K., Maruyama, S. (2009): Coesite and clinopyroxene exsolution lamellae in chromitites: in-situ ultrahigh-pressure evidence from podiform chromitites in the Luobusa ophiolite, southern Tibet. *Lithos*, **109**, 314–322.

Yang, J.S., Bai, W.J., Fang, Q.S., Yan, B.G., Shi, N.C., Ma, Z.S., Dai, M.Q., Xiong, M. (2003): Silicon rutile – an ultra-high pressure (UHP) mineral from an ophiolite. *Prog. Nat. Sci.*, **23**, 528–531.

Yang, J.S., Dobrzhinetskaya, L., Bai, W.J., Fang, Q.S., Robinson, P.T., Zhang, J.F., Green II, H.W. (2007): Diamond- and coesite-bearing chromitites from the Luobusa ophiolite, Tibet. *Geology*, **35**, 875–878.

Yang, J.S., Bai, W.J., Fang, Q.S., Rong, H. (2008): Ultrahigh-pressure minerals and new minerals from the Luobusa ophiolitic chromitites in Tibet: a review. *Acta Geosci. Sin.*, **29**, 263–274.

Yang, J.S., Robinson, P.T., Dilek, Y. (2014): Diamonds in ophiolites: a little-known diamond occurrence. *Elements*, **10**, 123–126.

Yang, J.S., Meng, F., Xu, S., Robinson, P.T., Dilek, Y., Makeyev, A.B., Wirth, R., Wiedenbeck, M., Cliff, J. (2015a): Diamonds, native elements and metal alloys from chromitites of the Ray-Iz ophiolite of the Polar Urals. *Gondwana Res.*, **27**, 459–485.

Yang, J.S., Robinson, P.T., Dilek, Y. (2015b): Diamond-bearing ophiolites and their geological occurrence. *Episodes*, **38**, 344–364.

Zhang, D. & Duan, Z. (2009): A model for C–O–H fluid in the Earth's mantle. *Geochim. Cosmochim. Acta*, **73**, 2089–2102.

Zhang, R.Y., Yang, J.S., Ernst, W.G., Jahn, B.M., Iizuka, Y., Guo, G.L. (2016a): Discovery of in situ super-reducing, ultrahigh-pressure phases in the Luobusa ophiolitic chromitites, Tibet: new insights into the deep upper mantle and mantle transition zone. *Am. Mineral.*, **101**, 1285–1294.

Zhang, C., Liu, C.Z., Wu, F.Y., Zhang, L.L., Ji, W.Q. (2016b): Geochemistry and geochronology of mafic rocks from the Luobusa ophiolite, *South Tibet. Lithos*, **245**, 93–108.

Zhang, Y.F., Jin, Z.M., Griffin, W.L., Wang, C., Wu, Y. (2017): High-pressure experiments provide insights into the Mantle Transition Zone history of chromitite in Tibetan ophiolites. *Earth Planet. Sci. Lett.*, **463**, 151–158.

Zhong, L.F., Xia, B., Zhang, Y.Q., Wang, R., Wei, D.L., Yang, Z.Q. (2006): SHRIMP age determination of the diabase in Luobusa ophiolite, southern Xizang (Tibet). *Geol. Rev.*, **52**, 224–229 (in Chinese with English abstract).

Zhou, M.F., Robinson, P.T., Malpas, J., Li, Z.J. (1996): Podiform chromitites in the Luobusa ophiolite (southern Tibet) implications for melt-rock interaction and chromite segregation in the upper mantle. *J. Petrol.*, **37**, 3–21.

Zhou, M.F., Robinson, P.T., Malpas, J., Edwards, S.J., Qi, L. (2005): REE and PGE geochemical constraints on the formation of dunites in the Luobusa ophiolite, southern Tibet. *J. Petrol.*, **46**, 615–639.

Zhou, M.F., Robinson, P.T., Su, B.X., Gao, J.F., Li, J.W., Yang, J.S., Malpas, J. (2014): Compositions of chromite, associated minerals, and parental magmas of podiform chromite deposits: the role of slab contamination of asthenospheric melts in suprasubduction zone environments. *Gondwana Res.*, **26**, 262–283.

Received 3 December 2016
Modified version received 8 March 2017
Accepted 25 March 2017